

A SELF-CONSISTENT MODEL OF THE CORONAL HEATING AND SOLAR WIND ACCELERATION INCLUDING COMPRESSIBLE AND INCOMPRESSIBLE HEATING PROCESSES

MUNEHITO SHODA¹, TAKAAKI YOKOYAMA¹, AND TAKERU K. SUZUKI²

¹Department of Earth and Planetary Science, The University of Tokyo, Hongo, Bunkyo-ku, Tokyo, 113-0033, Japan

²School of Arts & Sciences, The University of Tokyo, 3-8-1, Komaba, Meguro, Tokyo, 153-8902, Japan

ABSTRACT

We propose a novel one-dimensional model that includes both shock and turbulence heating and qualify how these processes contribute to heating the corona and driving the solar wind. Compressible MHD simulations allow us to automatically consider shock formation and dissipation, while turbulent dissipation is modeled via a one-point closure based on Alfvén wave turbulence. Numerical simulations were conducted with different photospheric perpendicular correlation lengths λ_0 , which is a critical parameter of Alfvén wave turbulence, and different root-mean-square photospheric transverse-wave amplitudes δv_0 . For the various λ_0 , we obtain a low-temperature chromosphere, high-temperature corona, and supersonic solar wind. Our analysis shows that turbulence heating is always dominant when $\lambda_0 \lesssim 1$ Mm. This result does not mean that we can ignore the compressibility because the analysis indicates that the compressible waves and their associated density fluctuations enhance the Alfvén wave reflection and therefore the turbulence heating. The density fluctuation and the cross helicity are strongly affected by λ_0 , while the coronal temperature and mass loss rate depend weakly on λ_0 .

Keywords: magnetohydrodynamic(MHD) — methods:numerical — solar wind — Sun:corona

1. INTRODUCTION

The mechanism sustaining the high-temperature corona (Edlén 1943) and solar wind (Parker 1958; Velli 1994) is still under investigation. Currently, it is widely accepted that the original energy source lies in the photospheric convective motion and its interaction with magnetic fields (Alfvén 1947; Osterbrock 1961; Steiner et al. 1998; van Ballegooijen et al. 1998; Fujimura & Tsuneta 2009; Kato et al. 2011, 2016). Since the existence of Alfvén waves is indicated by in-situ observations (Belcher & Davis 1971; Bale et al. 2005) and remote sensing (De Pontieu et al. 2007; Tomczyk et al. 2007; Okamoto & De Pontieu 2011; McIntosh et al. 2011; Thurgood et al. 2014), Alfvén-wave-driven models of the coronal heating (Barnes 1969; Cranmer et al. 1999) and solar wind acceleration (Belcher 1971; Jacques 1977) have been studied. Such models can explain the heating of both the coronal holes (Hollweg 1986; Suzuki & Inutsuka 2005; Verdini et al. 2010; Lionello et al. 2014; Matsumoto & Suzuki 2014; van Ballegooijen & Asgari-Targhi 2016) and coronal loops (Moriyasu et al. 2004; Antolin et al. 2008; van Ballegooijen et al. 2011; Verdini et al. 2012b). Some models can explain the formation of both fast and slow solar winds (Suzuki & Inutsuka 2006; Cranmer et al. 2007) by varying the expansion factor

(Wang & Sheeley 1990; Arge & Pizzo 2000).

To better model the corona and solar wind, the Alfvén wave propagation and dissipation needs to be solved precisely because the obtained structure is dependent on the heating distribution, that is, heating below and above the sonic point leads to slow and fast wind, respectively (Hansteen & Velli 2012). To take into account heating mechanisms such as parametric decay (Del Zanna et al. 2001, 2015; Shi et al. 2017), Alfvén wave turbulence (Iroshnikov 1964; Kraichnan 1965; Velli et al. 1989; Goldreich & Sridhar 1995; Matthaeus et al. 1999) and phase mixing (Heyvaerts & Priest 1983), we need to solve the three-dimensional compressible MHD equations with a sufficiently high resolution. However, due to its numerical difficulty and physical complexity, no models have ever included all the heating processes. To simplify the physics and reduce the computational cost, reduced MHD models have frequently been used (Matthaeus et al. 1999; Dmitruk et al. 2002; Oughton et al. 2006; Cranmer et al. 2007; Verdini et al. 2009; Chandran & Hollweg 2009; Verdini et al. 2010; Perez & Chandran 2013; Lionello et al. 2014; van Ballegooijen & Asgari-Targhi 2016). In such models, Alfvén wave turbulence driven by partial wave reflection (Ferraro & Plumpton 1958; Heinemann & Olbert

1980; An et al. 1990; Velli 1993; Hollweg & Isenberg 2007) is the only heating process. Some reflection-driven Alfvén wave turbulence models self-consistently succeed in explaining the coronal heating and solar wind accelerations (Crammer et al. 2007; Verdini et al. 2010). Recent 3D models, however, indicate that, under a smooth background field, turbulence cannot supply enough energy to sustain the corona (Perez & Chandran 2013; van Ballegoijen & Asgari-Targhi 2017). This indicates that we need to take into account the compressibility of plasma. In fact, compressible MHD models excluding Alfvén wave turbulence also succeed in generating the corona and solar wind (Suzuki 2004; Suzuki & Inutsuka 2005) based on shock heating. To summarize these recent studies, we need to solve for both shock (compressibility) and turbulence to achieve realistic models. In this study, to solve both shock and turbulence heating without expensive numerical cost, we constructed a new 1D model of the coronal heating and solar wind acceleration. We solve the 1D compressible MHD equations to include shock formation and dissipation, and a one-point closure model is incorporated to include turbulence heating. The one-dimensionality and the resulting low numerical cost enable us to conduct a parameter survey to achieve a better understanding of the relevant physics. In this study, we investigate which type of heating is dominant in the corona and solar wind.

The remainder of this paper is organized as follows. In Section 2, we discuss how to incorporate turbulent dissipation into one-dimensional MHD equations. The basic equations and numerical solver are also described in this section. The results are shown in Section 3, and we summarize the paper with a discussion in Section 4.

2. METHOD

2.1. Phenomenological terms of Alfvén wave turbulence

We consider a one-dimensional system with its coordinate curved along the background flux tube. We denote the coordinate along the tube by r ; therefore, $\partial/\partial r \neq 0$. In this case, following Suzuki & Inutsuka (2005, 2006), the basic equations for the transverse velocity \mathbf{v}_\perp and magnetic field \mathbf{B}_\perp are given as

$$\rho \frac{d}{dt} (\sqrt{A} \mathbf{v}_\perp) = \frac{B_r}{4\pi} \frac{\partial}{\partial r} (\sqrt{A} \mathbf{B}_\perp), \quad (1)$$

$$\frac{\partial}{\partial t} \mathbf{B}_\perp = \frac{1}{\sqrt{A}} \frac{\partial}{\partial r} \left[\sqrt{A} (\mathbf{v}_\perp B_r - v_r \mathbf{B}_\perp) \right], \quad (2)$$

where, in this subsection, we use A instead of $r^2 f$ to denote the cross section of the tube. d/dt represents the Lagrangian derivative: $d/dt = \partial/\partial t + v_r \partial/\partial r$. Using the mass conservation and solenoidal condition,

$$\frac{d}{dt} \rho + \frac{\rho}{A} \frac{\partial}{\partial r} (A v_r) = 0, \quad \frac{\partial}{\partial r} (A B_r) = 0, \quad (3)$$

and taking into account the turbulent diffusivity, the equations for \mathbf{v}_\perp and \mathbf{B}_\perp are written as

$$\begin{aligned} \frac{\partial}{\partial t} (\rho \mathbf{v}_\perp A^{3/2}) + \left[\left(\rho v_r \mathbf{v}_\perp - \frac{1}{4\pi} B_r \mathbf{B}_\perp \right) A^{3/2} \right] \\ = -\hat{\eta}_1 \cdot \rho \mathbf{v}_\perp A^{3/2} - \hat{\eta}_2 \cdot \sqrt{\frac{\rho}{4\pi}} \mathbf{B}_\perp A^{3/2}, \end{aligned} \quad (4)$$

$$\begin{aligned} \frac{\partial}{\partial t} (\mathbf{B}_\perp A^{1/2}) + \frac{\partial}{\partial r} \left[(v_r \mathbf{B}_\perp - \mathbf{v}_\perp B_r) A^{1/2} \right] \\ = -\hat{\eta}_1 \cdot \mathbf{B}_\perp A^{1/2} - \hat{\eta}_2 \cdot \sqrt{4\pi \rho} \mathbf{v}_\perp A^{1/2}, \end{aligned} \quad (5)$$

where $\hat{\eta}_1$ and $\hat{\eta}_2$ are diagonal matrices whose components are given as

$$\hat{\eta}_1 = \begin{pmatrix} \frac{c_d}{4\lambda} (|\zeta_x^+| + |\zeta_x^-|) & 0 \\ 0 & \frac{c_d}{4\lambda} (|\zeta_y^+| + |\zeta_y^-|) \end{pmatrix}, \quad (6)$$

$$\hat{\eta}_2 = \begin{pmatrix} \frac{c_d}{4\lambda} (|\zeta_x^+| - |\zeta_x^-|) & 0 \\ 0 & \frac{c_d}{4\lambda} (|\zeta_y^+| - |\zeta_y^-|) \end{pmatrix}, \quad (7)$$

where λ is the correlation length perpendicular to the mean field, x and y denote the two transverse components, and ζ represents the Elsässer variables (Elsasser 1950) given by

$$\zeta^\pm = \mathbf{v}_\perp \mp \frac{\mathbf{B}_\perp}{\sqrt{4\pi\rho}}. \quad (8)$$

Physically, $\hat{\eta}_1$ represents a simple dissipation by turbulence, while $\hat{\eta}_2$ comes from a relaxation process called dynamic alignment (Dobrowolny et al. 1980; Stribling & Matthaeus 1991). In fact, $\hat{\eta}_2$ arises only for imbalanced turbulence (Beresnyak & Lazarian 2008; Chandran 2008).

Here, we show that, as long as the density and radial velocity are time-independent as is often assumed, Eqs. (4) and (5) are consistent with the common Alfvén wave turbulence term. Introducing $\mathbf{b} = \mathbf{B}/\sqrt{4\pi\rho}$, we can rewrite eq.s (4) and (5) as

$$\begin{aligned} \frac{\partial}{\partial t} \mathbf{v}_\perp + v_r \frac{\partial}{\partial r} \mathbf{v}_\perp - b_r \frac{\partial}{\partial r} \mathbf{b}_\perp \\ + v_r \mathbf{v}_\perp \frac{\partial}{\partial r} \ln(A^{1/2}) - b_r \mathbf{b}_\perp \frac{\partial}{\partial r} \ln(\rho^{1/2} A^{1/2}) \\ = -\hat{\eta}_1 \cdot \mathbf{v}_\perp - \hat{\eta}_2 \cdot \mathbf{b}_\perp, \end{aligned} \quad (9)$$

$$\begin{aligned} \frac{\partial}{\partial t} \mathbf{b}_\perp + v_r \frac{\partial}{\partial r} \mathbf{b}_\perp - b_r \frac{\partial}{\partial r} \mathbf{v}_\perp \\ + b_r \mathbf{v}_\perp \frac{\partial}{\partial r} \ln(A^{1/2}) - v_r \mathbf{b}_\perp \frac{\partial}{\partial r} \ln(\rho^{1/2} A^{1/2}) \\ = -\hat{\eta}_1 \cdot \mathbf{b}_\perp - \hat{\eta}_2 \cdot \mathbf{v}_\perp. \end{aligned} \quad (10)$$

These equations are written in Elsässer variables as

$$\begin{aligned} & \frac{\partial}{\partial t} \zeta^\pm + (v_r \pm b_r) \frac{\partial}{\partial r} \zeta^\pm, \\ & -\zeta^\pm (v_r \mp b_r) \frac{\partial}{\partial r} \ln(\rho^{1/4}) + \zeta^\mp (v_r \mp b_r) \frac{\partial}{\partial r} \ln(\rho^{1/4} A^{1/2}) \\ & = -\hat{\eta}^\mp \cdot \zeta^\pm, \end{aligned} \quad (11)$$

where

$$\hat{\eta}^\mp = \hat{\eta}_1 \mp \hat{\eta}_2 = \begin{pmatrix} \frac{c_d}{2\lambda} |\zeta_x^\mp| & 0 \\ 0 & \frac{c_d}{2\lambda} |\zeta_y^\mp| \end{pmatrix}. \quad (12)$$

Note that v_r and b_r represent the background flow speed and the Alfvén velocity, respectively. The left hand side of Eq. (11) is identical to Eqs. (4a) and (4b) in [Heinemann & Olbert \(1980\)](#). The right hand side is equivalent to the Alfvén wave turbulence term approximated as ([Dobrowolny et al. 1980](#); [Hossain et al. 1995](#); [Matthaeus et al. 1999](#))

$$-(\zeta^\mp \cdot \nabla) \zeta^\pm \sim -c_d \frac{Z^\mp}{2\lambda} \zeta^\pm, \quad (13)$$

where Z^\mp is the rms amplitude of ζ^\mp , which is, following [Chandran & Hollweg \(2009\)](#) and [Lionello et al. \(2014\)](#), approximated by $|\zeta^\mp|$ in this study. $\tau_{\text{turb}}^\pm \sim \lambda/|\zeta^\mp|$ represents the timescale of the turbulence. The turbulence term $-\hat{\eta}^\mp \cdot \zeta^\pm$ arises only when there exist counter-propagating Alfvén waves ([Iroshnikov 1964](#); [Kraichnan 1965](#)). The choice of c_d is not trivial. Because the reflection timescale τ_{ref} must be smaller than the nonlinear timescale τ_{nl} to sustain the turbulence ([Dmitruk & Matthaeus 2003](#)), [Oughton et al. \(2006\)](#) and [Cranmer et al. \(2007\)](#) evaluated c_d as a function of the nonlinear timescale $\tau_{\text{nl}} = \tau_{\text{turb}}^\pm$ and the reflection timescale $\tau_{\text{ref}} = \nabla \cdot \mathbf{V}_A$, which gives $c_d = 0$ for $\tau_{\text{nl}}/\tau_{\text{ref}} \rightarrow \infty$ and $c_d = 1$ for $\tau_{\text{nl}}/\tau_{\text{ref}} \rightarrow 0$. Meanwhile, [Dmitruk et al. \(2002\)](#), [Verdini & Velli \(2007\)](#), [Chandran & Hollweg \(2009\)](#), [Verdini et al. \(2010\)](#), and [Lionello et al. \(2014\)](#) simply assume $c_d = 1$. Both models give similar results for the heating and acceleration, because c_d is approximately unity for the main heating region in both cases.

However, it has recently been pointed out by [van Ballegooijen et al. \(2011\)](#) and [van Ballegooijen & Asgari-Targhi \(2016\)](#) that this formulation overestimates the turbulent dissipation than the value obtained from 3D calculations. [Perez & Chandran \(2013\)](#) report that the heating rate calculated via 3D RMHD simulations is smaller compared to the required value. [van Ballegooijen & Asgari-Targhi \(2017\)](#) conclude that $c_d = 0.1$ gives a better approximation for the heating rate. Therefore, we use $c_d = 0.1$ in this study. Note that the actual value or function of c_d should have a

complex form that depends on the structure of magnetic field and power spectrum, and thus c_d is also a free parameter. However, because increasing c_d is mathematically equivalent with decreasing λ , we fixed c_d with a reasonable value by [van Ballegooijen & Asgari-Targhi \(2017\)](#) and changed λ in this study.

2.2. Basic equations

In addition to Eqs. (4) and (5), we solve the mass conservation equation, the equation of radial motion, and the energy equation. The basic equations in conservation form are

$$\frac{\partial}{\partial t} (\rho r^2 f) + \frac{\partial}{\partial r} (\rho v_r r^2 f) = 0, \quad (14)$$

$$\begin{aligned} & \frac{\partial}{\partial t} (\rho v_r r^2 f) + \frac{\partial}{\partial r} \left[\left(\rho v_r^2 + p + \frac{\mathbf{B}_\perp^2}{8\pi} \right) r^2 f \right] \\ & = \left(p + \frac{\rho v_\perp^2}{2} \right) \frac{d}{dr} (r^2 f) - \rho g r^2 f, \end{aligned} \quad (15)$$

$$\begin{aligned} & \frac{\partial}{\partial t} (\rho \mathbf{v}_\perp r^3 f^{3/2}) + \frac{\partial}{\partial r} \left[\left(\rho v_r \mathbf{v}_\perp - \frac{B_r \mathbf{B}_\perp}{4\pi} \right) r^3 f^{3/2} \right] \\ & = -\hat{\eta}_1 \cdot \rho \mathbf{v}_\perp r^3 f^{3/2} - \hat{\eta}_2 \cdot \sqrt{\frac{\rho}{4\pi}} \mathbf{B}_\perp r^3 f^{3/2}, \end{aligned} \quad (16)$$

$$\begin{aligned} & \frac{\partial}{\partial t} (\mathbf{B}_\perp r \sqrt{f}) + \frac{\partial}{\partial r} \left[(\mathbf{B}_\perp v_r - B_r \mathbf{v}_\perp) r \sqrt{f} \right] \\ & = -\hat{\eta}_1 \cdot \mathbf{B}_\perp r \sqrt{f} - \hat{\eta}_2 \cdot \sqrt{4\pi \rho} \mathbf{v}_\perp r \sqrt{f}, \end{aligned} \quad (17)$$

$$\frac{d}{dr} (B_r r^2 f) = 0, \quad (18)$$

$$\begin{aligned} & \frac{\partial}{\partial t} \left[\left(e + \frac{1}{2} \rho v^2 + \frac{\mathbf{B}^2}{8\pi} \right) r^2 f \right] \\ & + \frac{\partial}{\partial r} \left[\left(e + p + \frac{1}{2} \rho v^2 + \frac{\mathbf{B}_\perp^2}{4\pi} \right) v_r r^2 f - B_r \frac{\mathbf{B}_\perp \cdot \mathbf{v}_\perp}{4\pi} r^2 f \right] \\ & = r^2 f (-\rho g v_r + Q_{\text{rad}} + Q_{\text{cond}}), \end{aligned} \quad (19)$$

$$e = \frac{p}{\gamma - 1}, \quad p = \frac{\rho k_B T}{\mu m_H}, \quad (20)$$

where r is the heliocentric distance and f is the expansion factor of the flux tube ([Kopp & Holzer 1976](#); [Wang & Sheeley 1990](#)). See [Shoda & Yokoyama \(2018\)](#) for derivation. Note that Eqs. (16) and (17) are equivalent to Eqs. (4) and (5). Q_{rad} and Q_{cond} denote the radiative cooling and thermal conduction, respectively. The gravitational acceleration is $g = 2.74 \times 10^4 (r/R_{\text{Sun}})^{-2} \text{ cm s}^{-2}$. We assume that the solar atmosphere is composed of only hydrogen. μ is given as a function of density so that $\mu = 1$ in the photosphere and low chromosphere and $\mu = 0.5$ in the high chromosphere and corona. We ignored the dependence of μ on temperature for simplicity. Because we are interested in the coronal physics, and $\mu = 0.5$ (fully ionized) for coronal mass density, our assumption should not affect the numerical results.

Following [Suzuki & Inutsuka \(2005\)](#), we assume a two-step super-radial expansion of the flux tube such that

$$f = \frac{f_{\max,1} \exp\left(\frac{r-R_1}{\sigma_1}\right) + f_1}{\exp\left(\frac{r-R_1}{\sigma_1}\right) + 1} \cdot \frac{f_{\max,2} \exp\left(\frac{r-R_2}{\sigma_2}\right) + f_2}{\exp\left(\frac{r-R_2}{\sigma_2}\right) + 1}, \quad (21)$$

where

$$f_1 = 1 - (f_{\max,1} - 1) \exp\left(\frac{R_{\text{Sun}} - R_1}{\sigma_1}\right),$$

$$f_2 = 1 - (f_{\max,2} - 1) \exp\left(\frac{R_{\text{Sun}} - R_2}{\sigma_2}\right).$$

The first and second terms represent the chromospheric and coronal expansions, respectively. We assume that the first expansion is near $r - R_{\text{Sun}} = 1$ Mm with a length scale of $\sigma_1 = 0.25$ Mm while the second is near $r - R_{\text{Sun}} = 200$ Mm with a length scale of $\sigma_2 = 350$ Mm. The expansion factors are $f_{\max,1} = 120$ and $f_{\max,2} = 4$. The background magnetic field is calculated from f as

$$B_r = B_{r,0} \left(\frac{r}{R_{\text{Sun}}}\right)^{-2} f^{-1}. \quad (22)$$

The correlation length is assumed to increase with the expansion of the flux tube ([Dmitruk et al. 2002](#)). In addition, to restrict the Alfvén wave turbulence to the corona ([Cranmer et al. 2007](#); [Verdini et al. 2010](#)), we formulate λ such that

$$\lambda = \lambda_0 \sqrt{\frac{B_{r,0}}{B_r}} \max\left(1, \frac{\rho}{\rho_{\text{cor},1}}\right), \quad (23)$$

where $\rho_{\text{cor},1} = 10^{-16}$ g cm⁻³. This results in a turbulent dissipation slow enough to be negligible in the chromosphere. Note that some models indicate that the Alfvén wave turbulence is active also in the chromosphere ([van Ballegooijen et al. 2011](#); [Verdini et al. 2012b](#)). The purpose of this assumption is to compare our results to those of previous studies; there is no physical justification to exclude chromospheric Alfvén wave turbulence.

Radiative cooling is a combination of optically thick L_{thick} and thin L_{thin} contributions and is given by

$$Q_{\text{rad}} = \xi L_{\text{thick}} + (1 - \xi) L_{\text{thin}}, \quad (24)$$

where

$$\xi = \max\left[0, \left(1 - \frac{\rho_{\text{cor},2}}{\rho}\right)\right]. \quad (25)$$

Here, $\rho_{\text{cor},2} = 5 \times 10^{-17}$ g cm⁻³. Following [Gudiksen & Nordlund \(2005\)](#), instead of solving the radiative transfer, we approximate the optically thick cooling by Newtonian cooling as

$$L_{\text{thick}} = -\frac{1}{\tau_{\text{thick}}} (e - e_0), \quad (26)$$

where

$$\tau_{\text{thick}} = 1 \times \left(\frac{\rho}{\rho_0}\right)^{-1} \text{ s}, \quad e_0 = \frac{1}{\gamma - 1} \frac{\rho k_B T_{\text{ref}}}{\mu m_H}. \quad (27)$$

Here, ρ_0 is the photospheric mass density and τ_{thick} denotes the timescale of the cooling. T_{ref} represents a reference temperature that sets $T_{\text{ref}} = 6000$ K at $r = R_{\text{Sun}}$ and monotonically decreases with r . As for L_{thin} , we use the following formula:

$$L_{\text{thin}} = -n_i n_e \Lambda(T), \quad n_i = n_e \frac{\rho}{m_H} \left(\frac{1}{\mu} - 1\right), \quad (28)$$

where we use an approximated loss function for $\Lambda(T)$ ([Sutherland & Dopita 1993](#); [Matsumoto & Suzuki 2014](#)).

In the chromosphere and low corona where the plasma is collisional, Spitzer-Härm conduction ([Spitzer & Härm 1953](#)) is applicable. However, in the solar wind, Spitzer-Härm conduction is inadequate due to the long mean free path, and thus free-streaming type conduction ([Hollweg 1974, 1976](#)) should be used instead. Because the free-streaming conductive flux is smaller than the Spitzer-Härm conductive flux, to mimic the transition to free-streaming conduction, we formulate the conductive heating Q_{cond} and conductive flux q_{cond} such that

$$Q_{\text{cond}} = -\frac{1}{r^2 f} \frac{\partial}{\partial r} (\alpha q_{\text{cond}} r^2 f) \quad (29)$$

where

$$q_{\text{cond}} = -\kappa T^{5/2} \frac{\partial T}{\partial r}, \quad \alpha = \max\left(1, \frac{\rho}{\rho_{\text{sw}}}\right) \quad (30)$$

where $\rho_{\text{sw}} = 10^{-22}$ g cm⁻³ and $\kappa = 10^{-6}$ in CGS-Gaussian unit. α represents the flux quenching in the solar wind ($\rho < \rho_{\text{sw}}$).

2.3. Boundary conditions and schemes

The basic equations are solved from the bottom (photosphere) up to 0.5 au using 13000 non-uniform grid points. A static atmosphere with a temperature of 10000 K is used as the initial condition ([Suzuki & Inutsuka 2005](#)). The photospheric boundary conditions are as follows. The density, temperature, and radial magnetic field are fixed to $\rho_0 = 10^{-7}$ g cm⁻³, $T_0 = 6000$ K, and $B_{r,0} = 1000$ G, respectively. The free boundary condition is applied to the radial velocity at the photosphere. The transverse velocity and magnetic field with pink-noise spectra are given at the photosphere so that upward waves are excited:

$$\mathbf{v}_{\perp,0} \propto \int_{2\pi f_l}^{2\pi f_h} d\omega \omega^{-1/2} \sin(\omega t + \phi(\omega)), \quad (31)$$

$$\mathbf{B}_{\perp,0} = -\sqrt{4\pi\rho_0} \mathbf{v}_{\perp,0}, \quad (32)$$

where $f_l = 10^{-3}$ Hz and $f_h = 10^{-2}$ Hz. ϕ is a random function of ω . The photospheric correlation

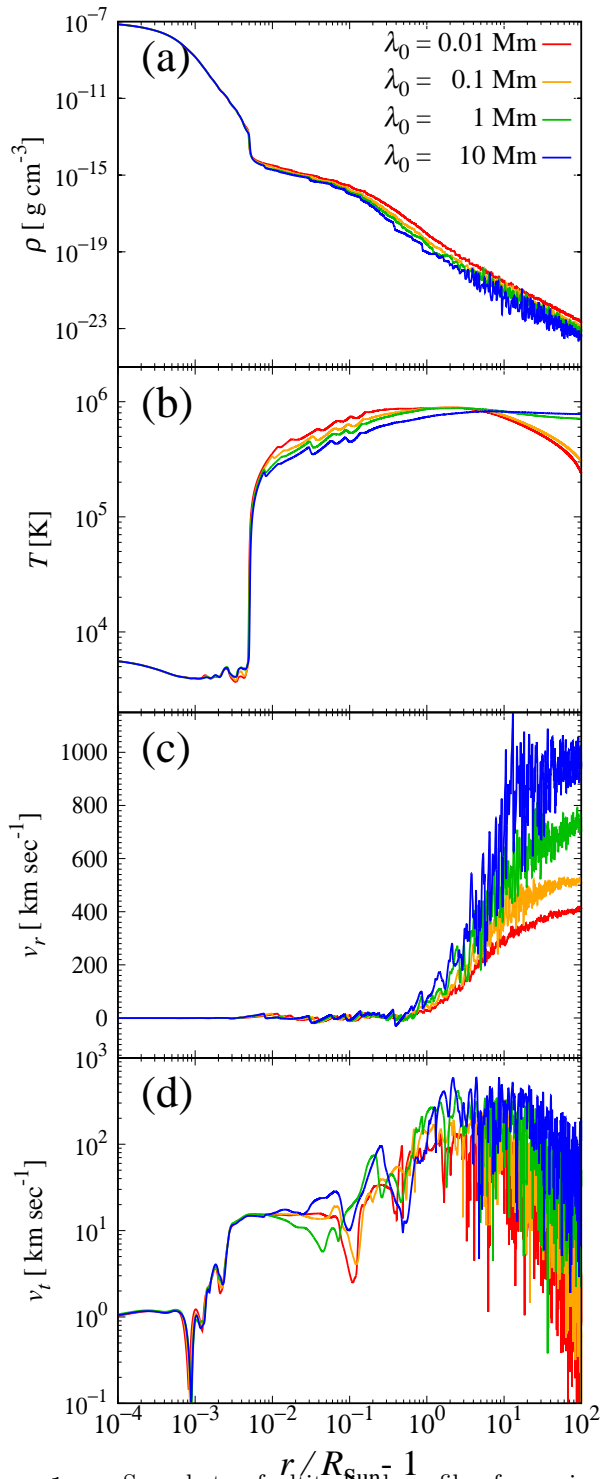


Figure 1. Snapshots of altitudinal profiles for various λ_0 . The mass density, temperature, radial velocity and transverse velocity are shown from the top to bottom. The red, orange, green and blue lines indicate $\lambda_0 = 0.01$ Mm, $\lambda_0 = 0.1$ Mm, $\lambda_0 = 1$ Mm, and $\lambda_0 = 10$ Mm, respectively.

length λ_0 and the root-mean-square value of $|\mathbf{v}_{\perp,0}|$ denoted by δv_0 are the free parameters in this study. As

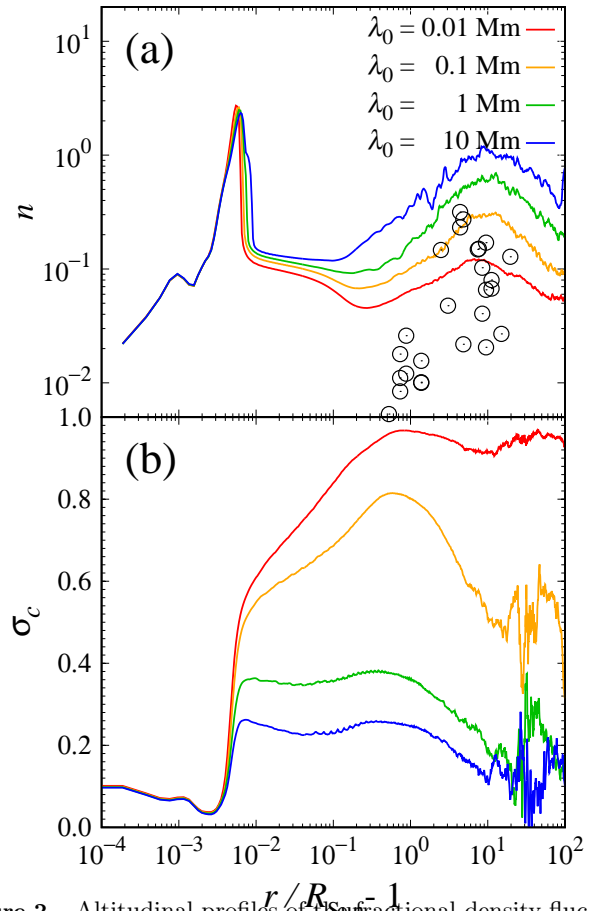


Figure 2. Altitudinal profiles of the fractional density fluctuation n and the normalized cross helicity σ_c . Shown by the four lines are cases with $\lambda_0 = 0.01$ Mm (red), $\lambda_0 = 0.1$ Mm (orange), $\lambda_0 = 1$ Mm (green), and $\lambda_0 = 10$ Mm (blue). Black circles indicate the radio-wave observations by Miyamoto et al. (2014).

for the upper boundary condition, we apply the free boundary condition to every variable. Even though the transmitting boundary condition (Thompson 1987; Del Zanna et al. 2001; Suzuki & Inutsuka 2006) is likely better, we confirmed that the numerical result does not depend greatly on the boundary condition because a super-sonic and super-Alfvénic outflow is obtained as a final state. We solve the conservation law using an approximated Riemann solver (Miyoshi & Kusano 2005) with 2nd-order MUSCL reconstruction and 3rd-order TVD Runge-Kutta method (Shu & Osher 1988). Super time stepping method (Meyer et al. 2012, 2014) is applied to solve the Spitzer-type thermal conduction in Eq. (19), which drastically improves the calculation speed.

3. RESULT

3.1. Quasi-steady states for various λ_0

Figure 1 shows snapshots of the quasi-steady states for four cases with different λ_0 values. The photospheric transverse velocity is fixed to $\delta v_0 = 0.5 \text{ km s}^{-1}$. The panels show profiles of (a) the mass density, (b) temperature, (c) radial velocity, and (d) transverse velocity $v_t = |\mathbf{v}_\perp|$. The four lines indicate the results with $\lambda_0 = 0.01 \text{ Mm}$ (red), $\lambda_0 = 0.1 \text{ Mm}$ (orange), $\lambda_0 = 1 \text{ Mm}$ (green), and $\lambda_0 = 10 \text{ Mm}$ (blue). In each case, a chromosphere and corona are generated with a sharp transition region in-between them and a solar wind with velocity $\gtrsim 400 \text{ km} \cdot \text{sec}^{-1}$ is formed.

Variations with respect to λ_0 will now be discussed. The solar wind has a different asymptotic velocity, which is larger for larger λ_0 (Figure 1c). The longer timescale of the turbulent dissipation makes waves propagate longer distances, giving rise to a faster solar wind because the heating in the supersonic region increases (Lamers & Cassinelli 1999; Hansteen & Velli 2012). The difference in the temperature profiles can also be interpreted via the location of the heating; the lower corona is hotter for smaller λ_0 , while the wind is hotter for larger λ_0 (Figure 1b). As for the wave amplitudes (Figure 1d), the four cases show a similar trend. We see $v_t = 10\text{--}30 \text{ km s}^{-1}$ near the transition region and low corona, which is consistent with the observational values (De Pontieu et al. 2007; McIntosh et al. 2011; Thurgood et al. 2014). An increasing trend of v_t up to $r/R_{\text{Sun}} - 1 \sim 3$ is seen in every case and is consistent with recent observation of non-thermal line broadening (Banerjee et al. 2009; Hahn & Savin 2013).

The density fluctuation and associated radial velocity fluctuation strongly depends on λ_0 . The large density fluctuation, which was observed also in previous studies (Suzuki & Inutsuka 2005, 2006), comes from a large amplitude MHD slow (acoustic) waves generated via the parametric decay instability (Sagdeev & Galeev 1969; Goldstein 1978; Del Zanna et al. 2001). This is clear from the relationship between the time-averaged fractional density fluctuation n and the normalized cross helicity σ_c defined as

$$n = \frac{1}{\bar{\rho}} \sqrt{(\rho - \bar{\rho})^2}, \quad (33)$$

$$\sigma_c = \frac{\overline{E^+} - \overline{E^-}}{\overline{E^+} + \overline{E^-}}, \quad E^\pm = \frac{1}{4} \rho \zeta^\pm{}^2, \quad (34)$$

where \overline{X} denotes the time average: $\overline{X} = 1/\tau \int_0^\tau dt X$, where $\tau = 1000 \text{ min}$. In Figure 2 we show the altitudinal profiles of n (a) and σ_c (b). It is clear, especially for large λ_0 , that the increasing n is associated with decreasing σ_c , which is consistent with the parametric decay instability.

According to Figure 2a, n has maxima near $r/R_{\text{Sun}} - 1 = 10^{-2}$ (the chromosphere and transition region) and $r/R_{\text{Sun}} = 10$ (the solar wind). The first

one results from sound waves nonlinearly generated from Alfvén waves via the wave pressure gradient (Hollweg 1971; Hollweg et al. 1982; Kudoh & Shibata 1999; Matsumoto & Shibata 2010). The sound waves are amplified due to the stratification and steepen to form shock waves (Carlsson & Stein 1992; Tian et al. 2014), leading to large density fluctuations. After a shock wave collides with the transition region, its energy is redistributed to the coronal shock wave, the upward motion of the transition region, and the chromospheric rarefaction wave (Hollweg 1982). This is the cause of the rapid decrease in n above the transition region. The second peak results from the decay instability, which enhances n and reduces σ_c due to backscattering (Malara et al. 2000; Del Zanna et al. 2001; Shoda & Yokoyama 2016).

The black circles in Figure 2a indicate radio-wave observations by Miyamoto et al. (2014) using *Akatsuki* (Nakamura et al. 2011). All four cases show an increasing trend for n with r in $0.1 < r/R_{\text{Sun}} - 1 \lesssim 10$, which is consistent with the observation. These observational data could underestimate the actual values because positive and negative density fluctuations, which cause radio scintillation, are canceled out in the integration along the line of sight. Therefore, even though our theoretical results exceed most of the observational data, this discrepancy is not a contradiction.

Even though the fluctuations in ρ and v_r has a large length scale typically of $0.1 R_{\text{Sun}}$, they are not observable by remote sensing because the intensity of that region is extremely low. In-situ observations would be the only way to detect the fluctuations, which is expected from *Parker Solar Probe* (Fox et al. 2016).

n and σ_c show different behaviors with different λ_0 . First, the magnitude of n near $r/R_{\text{Sun}} = 10$ is smaller for smaller λ_0 . This is likely because the growth rate and saturation level of the decay instability decrease due to smaller wave powers or because the decay instability itself is suppressed by the presence of turbulence. Second, the magnitude of σ_c in the corona and solar wind becomes smaller as λ_0 increases. This is a natural result of dynamic alignment (Dobrowolny et al. 1980; Stribling & Matthaeus 1991). Large σ_c observed in the fast solar wind near 1 au (Belcher & Davis 1971; Bavassano et al. 2000) likely results from small λ_0 ($\lambda_0 \lesssim 0.1 \text{ Mm}$) and the subsequent alignment. However, recent observations by CoMP reveal that a significant amount of reflected Alfvén waves exist in the low corona (Morton et al. 2015). According to Morton et al. (2015), the energy ratio E^-/E^+ is $0.5\text{--}1.0$, which is, in terms of σ_c , $0\text{--}0.3$. Thus, $\lambda_0 \gtrsim 1 \text{ Mm}$ is preferable to explain their observation. Explaining the cross helicity profile from the low corona up to the distant heliosphere $r \gtrsim 1 \text{ au}$ is beyond the scope of this study and remains

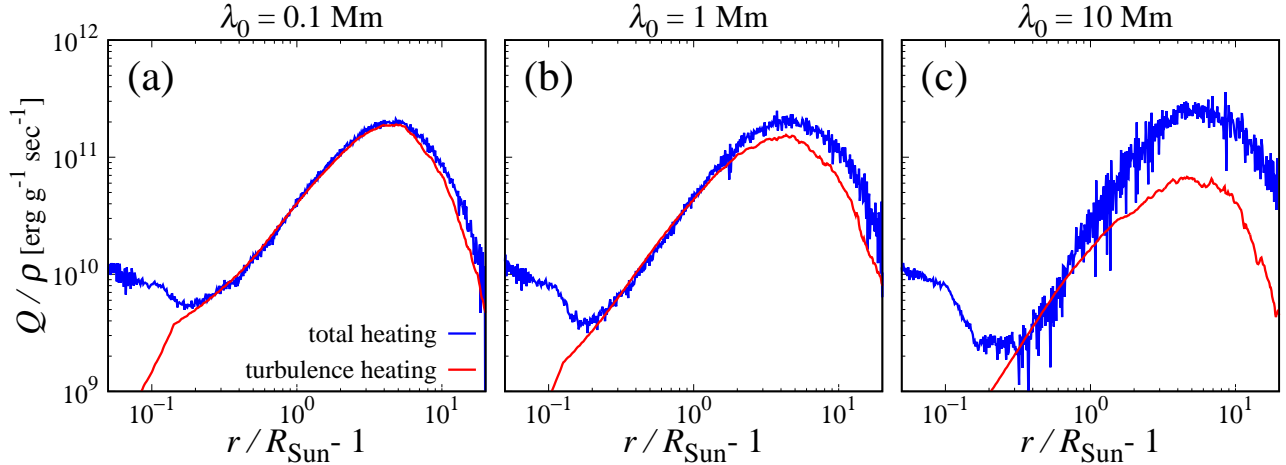


Figure 3. Altitudinal profiles of the time-averaged total heating (Q_{heat}/ρ : blue line) and turbulence heating (Q_{turb}/ρ : red line) for various λ_0 . The left, middle and right panels indicate $\lambda_0 = 0.1$ Mm, $\lambda_0 = 1$ Mm, and $\lambda_0 = 10$ Mm, respectively.

for future work.

3.2. Heating mechanism

To measure the heating, we use the energy equation written in the following manner (Cranmer et al. 2007).

$$\frac{\partial e}{\partial t} + v_r \frac{\partial e}{\partial r} + \frac{e+p}{r^2 f} \frac{\partial}{\partial r} (v_r r^2 f) = Q_{\text{rad}} + Q_{\text{cond}} + Q_{\text{heat}}, \quad (35)$$

where Q_{heat} is the heating by waves. This equation is derived from the basic equations. After a quasi-steady state is achieved, using time averaging, we obtain

$$\overline{Q_{\text{heat}}} = v_r \overline{\frac{\partial e}{\partial r}} + \frac{e+p}{r^2 f} \overline{\frac{\partial}{\partial r} (v_r r^2 f)} - Q_{\text{rad}} - Q_{\text{cond}}, \quad (36)$$

where we use $\overline{\partial e / \partial t} = 0$. We can calculate the total wave heating in this manner. Meanwhile, the turbulent heating Q_{turb} is analytically derived as (Verdini & Velli 2007; Cranmer et al. 2007)

$$Q_{\text{turb}} = \frac{1}{4} \rho \sum_{i=x,y} c_d \frac{|\zeta_i^+| |\zeta_i^-|^2 + |\zeta_i^-| |\zeta_i^+|^2}{\lambda}, \quad (37)$$

where x and y denote the components perpendicular to the background flux tube. In Figure 3, we show the time-averaged heating per unit mass $\overline{Q_{\text{heat}}}/\bar{\rho}$ (blue line) and $\overline{Q_{\text{turb}}}/\bar{\rho}$ (red line) for cases with the same wave amplitude ($\delta v_0 = 0.5$ km s $^{-1}$) and different correlation lengths ($\lambda_0 = 0.1$ Mm, 1 Mm, and 10 Mm). In every case, the heating per unit mass reaches $\sim 10^{11}$ erg g $^{-1}$ s $^{-1}$, showing that a sufficient amount of energy is supplied to sustain the coronal temperature. For $\lambda_0 \lesssim 0.1$ Mm, the turbulence heating is dominant

everywhere; meanwhile for $\lambda_0 \gtrsim 1$ Mm, the shock heating is comparably or more important in the extended corona and solar wind. Thus our first conclusion is that the dominant heating process is turbulence when $\lambda_0 \lesssim 1$ Mm. In particular, when $\lambda_0 \lesssim 0.1$ Mm, the shock heating is nearly negligible. What is interesting in this analysis is that, even though we apply small turbulence heating ($c_d = 0.1$), the sufficient amount of energy is supplied only by the turbulent heating when $\lambda_0 = 1$ Mm. In contrast, a reduced MHD calculation (Perez & Chandran 2013) gives a heating rate of at most $\sim 10^{10}$ erg g $^{-1}$ s $^{-1}$ when $\lambda_0 \sim 1$ Mm. The enhanced heating indicates that Alfvén wave reflection, which is the trigger of Alfvén wave turbulence, is activated due to the compressibility. This is possibly because of the presence of parametric decay or reflection driven by density fluctuations (Suzuki & Inutsuka 2006; van Ballegooijen & Asgari-Targhi 2016). In this regard, the compressibility can never be ignorable not only due to shock heating but also due to reflection enhancement.

3.3. Dependences on λ_0 and δv_0

Following Cranmer et al. (2007), we discuss the dependences of the asymptotic solar wind velocity, maximum coronal temperature and mass loss rate on λ_0 and δv_0 . We show in Figure 4 the time-averaged (a) wind velocity at $r = 0.5$ au, (b) maximum temperature and (c) mass loss rate.

According to Cranmer et al. (2007) and Verdini et al. (2010), the solar wind velocity tends to increase when λ_0 increases. This is observed in our result regardless of δv_0 . Cranmer et al. (2007) and Suzuki & Inutsuka (2006) also argue that the wind velocity decreases as δv_0 increases. This is evident for large λ_0 . As for

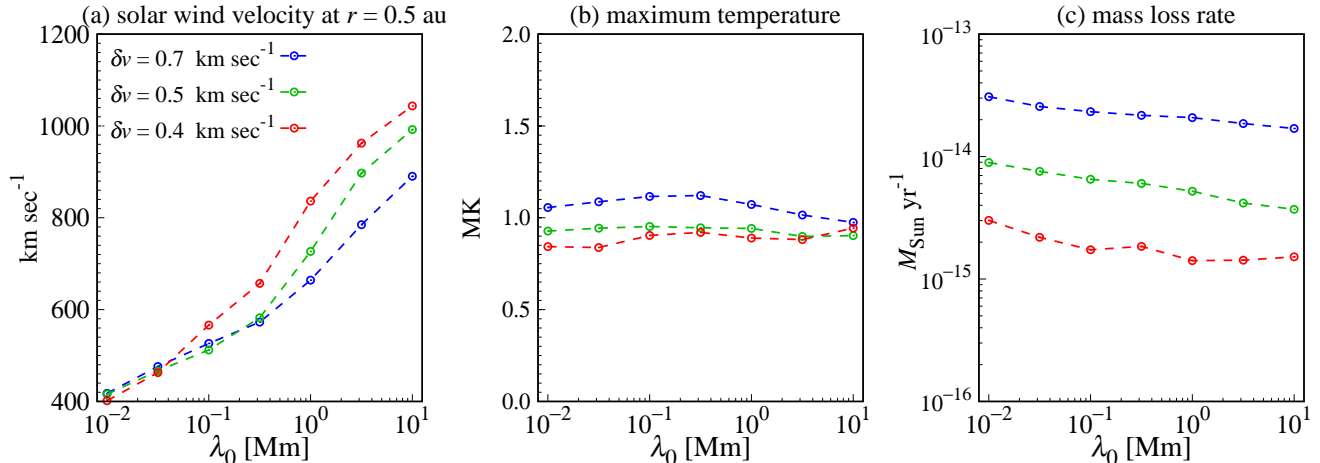


Figure 4. Time-averaged wind velocity at $r = 0.5$ au (left), maximum temperature (middle), and mass loss rate (right) for various λ_0 and δv_0 . The units for the vertical axes are km s^{-1} , MK, and $M_{\text{Sun}} \text{ yr}^{-1}$, respectively, where M_{Sun} is the solar mass. The horizontal axis shows λ_0 in unit of Mm. The red, green, and blue lines indicate $\delta v_0 = 0.4 \text{ km s}^{-1}$, 0.5 km s^{-1} , and 0.7 km s^{-1} , respectively.

small λ_0 , the wind velocity is nearly constant around $\sim 400 \text{ km s}^{-1}$, indicating that the solar wind is completely thermally driven (Parker 1958; Hartle & Sturrock 1968). The maximum temperature changes little with λ_0 and δv_0 as seen in Cranmer et al. (2007). Especially, the maximum temperature is almost constant with respect to λ_0 . This invariance is because the change in λ_0 is balanced by adjusting the fractional contributions from turbulence and shock heating. Indeed, the total heating rate per unit mass is nearly the same for different λ_0 values (Figure 3). Suppose that λ_0 becomes smaller and turbulent heating is enhanced. Due to the increase in the coronal gas pressure, the plasma becomes more incompressible, leading to the reduction of compressible heating. The mass loss rate is also independent of λ_0 , because it is almost independent of the heating location (Hansteen & Leer 1995). Meanwhile, the mass loss rate sensitively depends on δv_0 (Suzuki 2006; Cranmer et al. 2007); the cases with $\delta v_0 = 0.7 \text{ km s}^{-1}$ give approximately an order of magnitude larger mass loss rates than the cases with $\delta v_0 = 0.4 \text{ km s}^{-1}$, even though the energy input $\propto \delta v_0^2$ is only three times larger. This is mainly because the reflection of the Alfvén waves is suppressed for larger δv_0 ; a larger δv_0 gives higher coronal density and hotter corona because of the larger heating. The denser corona suppresses the wave reflection in the chromosphere because the density difference between the photosphere and the corona is smaller; the hotter corona suppresses the wave reflection in the corona because the scale height is larger there. These effects make a larger fraction of the input energy transmitted to the

corona and the solar wind region to drive denser wind (Suzuki et al. 2013). To summarize, our simulations obtain the same trends as those obtained by Cranmer et al. (2007). This is not trivial because we include compressible waves in the corona and solar wind and use different values for c_d .

4. SUMMARY & DISCUSSION

In this paper, we proposed a new 1D model of the coronal heating and solar wind acceleration. Our model is a hybrid model of a time-dependent compressible heating model (Suzuki & Inutsuka 2005) and an incompressible heating model (Lionello et al. 2014). Because both the compressible heating and incompressible heating are important in the corona and solar wind (Matsumoto & Suzuki 2014), our model likely gives a better result compared to previous studies. As shown in Figure 1, the corona and the solar wind are formed regardless of the photospheric correlation length λ_0 . The main heating mechanism is the turbulence heating (Figure 3), especially when $\lambda_0 \lesssim 1 \text{ Mm}$. This does not necessarily mean that the compressibility is negligible. The fact that we obtain sufficient amounts of turbulence heating even for $\lambda_0 = 1 \text{ Mm}$ despite small c_d ($c_d = 0.1$) indicates that the compressibility plays a role in the enhancement of Alfvén wave reflection and, as a result, turbulence heating via the parametric decay instability. The density fluctuation, cross helicity, and solar wind velocity are strongly affected by λ_0 (Figure 1, 2), while the maximum coronal temperature and mass loss rate are almost independent of λ_0 (Figure 4).

Our turbulence model is one of the simplest models currently in use, and there is much space for improvement. The turbulence term we used is derived from the reduced MHD equations (Hossain et al. 1995; Dmitruk et al. 2002). However, this treatment may not be applicable to our compressible MHD system. For a better modeling, the direct treatment of the compressible MHD turbulence (Grappin et al. 1993; Chandran 2005) may be a better approach. To discuss the spectral evolution in the wave-number space, a shell model (Buchlin & Velli 2007; Verdini et al. 2012a) is a possible extension to solve a large range of spatial scales.

The photospheric correlation length, λ_0 , should in principle be determined from the physical properties of the magneto-convection below the photosphere. According to Rempel (2014), the spatial power peak of the photospheric kinetic energy lies around $\lambda \sim 1$ Mm, while the magnetic energy is nearly flat for $0.1 \text{ Mm} \lesssim \lambda \lesssim 10 \text{ Mm}$. $\lambda \sim 1$ Mm is on the scale of granulation while $\lambda \sim 0.1$ Mm corresponds to the scale of intergranular sub-arcsec magnetic patches (Berger et al. 1995; Berger & Title 2001). If we simply assume that λ_0 is comparable to the energetic scale of the photospheric motion, $\lambda_0 = 1$ Mm is a reasonable choice. This assumption is equivalent to the idea that the swaying

motion of the flux tube is the main driver of transverse waves (Steiner et al. 1998). However, if the vortex flow inside the magnetic patches is the most energetic driver of transverse waves (van Ballegoijen et al. 2011), $\lambda_0 = 0.1$ Mm is preferable. Radiation MHD simulations indicate that the vortex size in the chromosphere is around $\lambda \sim 1$ Mm (Moll et al. 2012; Iijima & Yokoyama 2017). Therefore, the most preferable value of λ_0 lies between 0.1 Mm and 1 Mm, depending on the generation mechanism of waves. As discussed in Section 3.1, the coronal observation is consistent with $\lambda_0 \gtrsim 1$ Mm. Thus, $\lambda_0 \sim 1$ Mm is consistent with the photospheric wave driving and coronal wave observation, although the best choice for λ_0 should be investigated in detail from both aspects in future works.

M.S. is supported by Leading Graduate Course for Frontiers of Mathematical Sciences and Physics (FMSP) and Grant-in-Aid for JSPS Fellows. T.Y. is supported by JSPS KAKENHI Grant Number 15H03640. T.K.S. is supported in part by Grants-in-Aid for Scientific Research from the MEXT of Japan, 17H01105. Numerical calculations were in part carried out on PC cluster at Center for Computational Astrophysics, National Astronomical Observatory of Japan.

REFERENCES

- Alfvén, H. 1947, *MNRAS*, 107, 211
- An, C.-H., Suess, S. T., Moore, R. L., & Musielak, Z. E. 1990, *ApJ*, 350, 309
- Antolin, P., Shibata, K., Kudoh, T., Shiota, D., & Brooks, D. 2008, *ApJ*, 688, 669
- Arge, C. N., & Pizzo, V. J. 2000, *J. Geophys. Res.*, 105, 10465
- Bale, S. D., Kellogg, P. J., Mozer, F. S., Horbury, T. S., & Reme, H. 2005, *Physical Review Letters*, 94, 215002
- Banerjee, D., Pérez-Suárez, D., & Doyle, J. G. 2009, *A&A*, 501, L15
- Barnes, A. 1969, *ApJ*, 155, 311
- Bavassano, B., Pietropaolo, E., & Bruno, R. 2000, *J. Geophys. Res.*, 105, 15959
- Belcher, J. W. 1971, *ApJ*, 168, 509
- Belcher, J. W., & Davis, Jr., L. 1971, *J. Geophys. Res.*, 76, 3534
- Beresnyak, A., & Lazarian, A. 2008, *ApJ*, 682, 1070
- Berger, T. E., Schrijver, C. J., Shine, R. A., Tarbell, T. D., Title, A. M., & Scharmer, G. 1995, *ApJ*, 454, 531
- Berger, T. E., & Title, A. M. 2001, *ApJ*, 553, 449
- Buchlin, E., & Velli, M. 2007, *ApJ*, 662, 701
- Carlsson, M., & Stein, R. F. 1992, *ApJL*, 397, L59
- Chandran, B. D. G. 2005, *Physical Review Letters*, 95, 265004
- . 2008, *ApJ*, 685, 646
- Chandran, B. D. G., & Hollweg, J. V. 2009, *ApJ*, 707, 1659
- Cranmer, S. R., Field, G. B., & Kohl, J. L. 1999, *ApJ*, 518, 937
- Cranmer, S. R., van Ballegoijen, A. A., & Edgar, R. J. 2007, *ApJS*, 171, 520
- De Pontieu, B., et al. 2007, *Science*, 318, 1574
- Del Zanna, L., Matteini, L., Landi, S., Verdini, A., & Velli, M. 2015, *Journal of Plasma Physics*, 81, 325810102
- Del Zanna, L., Velli, M., & Londrillo, P. 2001, *A&A*, 367, 705
- Dmitruk, P., & Matthaeus, W. H. 2003, *ApJ*, 597, 1097
- Dmitruk, P., Matthaeus, W. H., Milano, L. J., Oughton, S., Zank, G. P., & Mullan, D. J. 2002, *ApJ*, 575, 571
- Dobrowolny, M., Mangeney, A., & Veltri, P. 1980, *Physical Review Letters*, 45, 144
- Edlén, B. 1943, *ZA*, 22, 30
- Elsasser, W. M. 1950, *Physical Review*, 79, 183
- Ferraro, C. A., & Plumpton, C. 1958, *ApJ*, 127, 459
- Fox, N. J., et al. 2016, *SSRv*, 204, 7
- Fujimura, D., & Tsuneta, S. 2009, *ApJ*, 702, 1443
- Goldreich, P., & Sridhar, S. 1995, *ApJ*, 438, 763
- Goldstein, M. L. 1978, *ApJ*, 219, 700
- Grappin, R., Velli, M., & Mangeney, A. 1993, *Physical Review Letters*, 70, 2190
- Gudiksen, B. V., & Nordlund, Å. 2005, *ApJ*, 618, 1020
- Hahn, M., & Savin, D. W. 2013, *ApJ*, 776, 78
- Hansteen, V. H., & Leer, E. 1995, *J. Geophys. Res.*, 100, 21577
- Hansteen, V. H., & Velli, M. 2012, *SSRv*, 172, 89
- Hartle, R. E., & Sturrock, P. A. 1968, *ApJ*, 151, 1155
- Heinemann, M., & Olbert, S. 1980, *J. Geophys. Res.*, 85, 1311
- Heyvaerts, J., & Priest, E. R. 1983, *A&A*, 117, 220
- Hollweg, J. V. 1971, *J. Geophys. Res.*, 76, 5155
- . 1974, *J. Geophys. Res.*, 79, 3845
- . 1976, *J. Geophys. Res.*, 81, 1649
- . 1982, *ApJ*, 257, 345
- . 1986, *J. Geophys. Res.*, 91, 4111
- Hollweg, J. V., & Isenberg, P. A. 2007, *Journal of Geophysical Research (Space Physics)*, 112, 8102
- Hollweg, J. V., Jackson, S., & Galloway, D. 1982, *SoPh*, 75, 35
- Hossain, M., Gray, P. C., Pontius, Jr., D. H., Matthaeus, W. H., & Oughton, S. 1995, *Physics of Fluids*, 7, 2886
- Iijima, H., & Yokoyama, T. 2017, *ApJ*, 848, 38
- Iroshnikov, P. S. 1964, *Soviet Ast.*, 7, 566

- Jacques, S. A. 1977, *ApJ*, 215, 942
- Kato, Y., Steiner, O., Hansteen, V., Gudiksen, B., Wedemeyer, S., & Carlsson, M. 2016, *ApJ*, 827, 7
- Kato, Y., Steiner, O., Steffen, M., & Suematsu, Y. 2011, *ApJL*, 730, L24
- Kopp, R. A., & Holzer, T. E. 1976, *SoPh*, 49, 43
- Kraichnan, R. H. 1965, *Physics of Fluids*, 8, 1385
- Kudoh, T., & Shibata, K. 1999, *ApJ*, 514, 493
- Lamers, H. J. G. L. M., & Cassinelli, J. P. 1999, *Introduction to Stellar Winds*, 452
- Lionello, R., Velli, M., Downs, C., Linker, J. A., Mikić, Z., & Verdini, A. 2014, *ApJ*, 784, 120
- Malara, F., Primavera, L., & Veltri, P. 2000, *Physics of Plasmas*, 7, 2866
- Matsumoto, T., & Shibata, K. 2010, *ApJ*, 710, 1857
- Matsumoto, T., & Suzuki, T. K. 2014, *MNRAS*, 440, 971
- Matthaeus, W. H., Zank, G. P., Oughton, S., Mullan, D. J., & Dmitruk, P. 1999, *ApJL*, 523, L93
- McIntosh, S. W., de Pontieu, B., Carlsson, M., Hansteen, V., Boerner, P., & Goossens, M. 2011, *Nature*, 475, 477
- Meyer, C. D., Balsara, D. S., & Aslam, T. D. 2012, *MNRAS*, 422, 2102
- . 2014, *Journal of Computational Physics*, 257, 594
- Miyamoto, M., et al. 2014, *ApJ*, 797, 51
- Miyoshi, T., & Kusano, K. 2005, *Journal of Computational Physics*, 208, 315
- Moll, R., Cameron, R. H., & Schüssler, M. 2012, *A&A*, 541, A68
- Moriyasu, S., Kudoh, T., Yokoyama, T., & Shibata, K. 2004, *ApJL*, 601, L107
- Morton, R. J., Tomczyk, S., & Pinto, R. 2015, *Nature Communications*, 6, 7813
- Nakamura, M., et al. 2011, *Earth, Planets, and Space*, 63, 443
- Okamoto, T. J., & De Pontieu, B. 2011, *ApJL*, 736, L24
- Osterbrock, D. E. 1961, *ApJ*, 134, 347
- Oughton, S., Dmitruk, P., & Matthaeus, W. H. 2006, *Physics of Plasmas*, 13, 042306
- Parker, E. N. 1958, *ApJ*, 128, 664
- Perez, J. C., & Chandran, B. D. G. 2013, *ApJ*, 776, 124
- Rempel, M. 2014, *ApJ*, 789, 132
- Sagdeev, R. Z., & Galeev, A. A. 1969, *Nonlinear Plasma Theory*
- Shi, M., Li, H., Xiao, C., & Wang, X. 2017, *ApJ*, 842, 63
- Shoda, M., & Yokoyama, T. 2016, *ApJ*, 820, 123
- Shoda, M., & Yokoyama, T. 2018, *ArXiv e-prints* [arXiv:1801.01245]
- Shu, C.-W., & Osher, S. 1988, *Journal of Computational Physics*, 77, 439
- Spitzer, L., & Härm, R. 1953, *Physical Review*, 89, 977
- Steiner, O., Grossmann-Doerth, U., Knölker, M., & Schüssler, M. 1998, *ApJ*, 495, 468
- Stribling, T., & Matthaeus, W. H. 1991, *Physics of Fluids B*, 3, 1848
- Sutherland, R. S., & Dopita, M. A. 1993, *ApJS*, 88, 253
- Suzuki, T. K. 2004, *MNRAS*, 349, 1227
- . 2006, *ApJL*, 640, L75
- Suzuki, T. K., Imada, S., Kataoka, R., Kato, Y., Matsumoto, T., Miyahara, H., & Tsuneta, S. 2013, *PASJ*, 65, 98
- Suzuki, T. K., & Inutsuka, S.-i. 2005, *ApJL*, 632, L49
- Suzuki, T. K., & Inutsuka, S.-I. 2006, *Journal of Geophysical Research (Space Physics)*, 111, 6101
- Thompson, K. W. 1987, *Journal of Computational Physics*, 68, 1
- Thurgood, J. O., Morton, R. J., & McLaughlin, J. A. 2014, *ApJL*, 790, L2
- Tian, H., et al. 2014, *ApJ*, 786, 137
- Tomczyk, S., McIntosh, S. W., Keil, S. L., Judge, P. G., Schad, T., Seeley, D. H., & Edmondson, J. 2007, *Science*, 317, 1192
- van Ballegooijen, A. A., & Asgari-Targhi, M. 2016, *ApJ*, 821, 106
- . 2017, *ApJ*, 835, 10
- van Ballegooijen, A. A., Asgari-Targhi, M., Cranmer, S. R., & DeLuca, E. E. 2011, *ApJ*, 736, 3
- van Ballegooijen, A. A., Nisenson, P., Noyes, R. W., Löfdahl, M. G., Stein, R. F., Nordlund, Å., & Krishnakumar, V. 1998, *ApJ*, 509, 435
- Velli, M. 1993, *A&A*, 270, 304
- . 1994, *ApJL*, 432, L55
- Velli, M., Grappin, R., & Mangeney, A. 1989, *Physical Review Letters*, 63, 1807
- Verdini, A., Grappin, R., Pinto, R., & Velli, M. 2012a, *ApJL*, 750, L33
- Verdini, A., Grappin, R., & Velli, M. 2012b, *A&A*, 538, A70
- Verdini, A., & Velli, M. 2007, *ApJ*, 662, 669
- Verdini, A., Velli, M., & Buchlin, E. 2009, *ApJL*, 700, L39
- Verdini, A., Velli, M., Matthaeus, W. H., Oughton, S., & Dmitruk, P. 2010, *ApJL*, 708, L116
- Wang, Y.-M., & Sheeley, Jr., N. R. 1990, *ApJ*, 355, 726